Nonlinear features of equatorial baroclinic Rossby waves detected in Topex altimeter observations

N. S. Glazman, A. Fabrikant (*), and A.M. Greysuk

Jet Propulsion Laboratory, California Institute of Technology, Pasadena CA 91109

Tel.: 818-354-7151, E-mail: reg@pacific.jpl.nasa.gov

(*) Department of Meteorology, Pennsylvania State University, University Park, PA 16802-5013

Using a recently proposed technique for statistical analysis of non-gridded satellite altimeter data, regime of equatorially-trapped baroclinic Rossby waves is studied. One-dimensional spatial and spatial-temporal autocorrelation functions of sea surface height (SSH) variations in the equatorial Pacific waveguide yield a broad spectrum of baroclinic Rossby waves and permit determination of their propagation velocity. The 1-d wavenumber spectrum of zonal variations is given by a power-law k^{-2} on scales from about 10^3 km to 10^4 km. We demonstrate that the observed wave regime exhibits features of soliton turbulence developing in the long baroclinic Rossby waves. However, being limited to second statistical moments, the present analysis does not allow us to rule out a possibility of weak wave turbulence.

October 2, 1995

1. Introduction

Baroclinic Rossby waves represent an important component of' equatorial wave dynamics. Of particular interest is the question about these waves nonlinearity. One of the goals of the present work is to detect manifestations of the nonlinear nature of equatorially trapped baroclinic Rossby waves.

Weakly-nonlinear long Rossby waves obey the KdV equation and, in a stationary regime, may form solitons (Boyd, 1980; Marshall and Boyd, 1987). When their amplitude is sufficiently large, the solitons acquire properties of westward propagating mid-latitude modons (Boyd, 1985). In particular, they carry a region of closed re-circulation - an important feature with respect to mass and heat transport in equatorial regions. A set of non-interacting solitons with randomly distributed amplitudes is referred to as soliton gas or soliton turbulence (Kingsep et al., 1973; D'yachenko et al., 1989). An alternative regime of nonlinear wave dynamics is represented by weak wave turbulence (Zakharov et al., 1992). Spectral cascades of energy, momentum and other quantities which are manifested in a cascade pattern in the surface topography are an important feature of this particular regime. In either case, the characteristic propagation speed of nonlinear waves is greater than that predicted by linear wave theory, and the wavenumber spectrum of sea surface height (SSH) zonal variations tends to be rather broad. One formal distinction between soliton and weak wave turbulence is the degree of phase coupling between individual Fourier components of the wave field: being weak for wave turbulence, this coupling is strong for solitons. Unfortunately, the present analysis does not allow us to estimate this coupling, although the wavenumber spectrum of zonal SSH variations and other properties of the wave field reported in section 5 suggest that the process is essentially non-linear.

Using a recently developed statistical approach (Glazman et al., 1995), we examine SSH variations in a narrow zonal channel centered on the Pacific equator. Sampling limitations related to the satellite orbit configuration determine the temporal and spatial

resolution of our analysis. As explained in sections 2 and 3, we can presently resolve variations with time scales greater than about 10 days and spatial scales starting at about 800 km. Wave motions with smaller scales are filtered out due to the averaging procedure described in section 3. In order to emphasize this filtering property, a remote analogy between our statistical approach and the quasi-geostrophic approximation may be pointed out. While insufficient for studies of baroclinic Kelvin and all types of barotropic waves, our technique is adequate for analysis of long baroclinic Rossby waves. Indeed, as shown in Fig. 1, the period of the first meridional, first baroclinic Rossby mode is at least three times as large as the corresponding Kelvin wave period for the same wavelength - i.e., is always greater than 35 days.

As an alternative to statistical analysis, large-scale zonal motion in equatorial regions could be deduced from a sequence of SSH contour plots by tracking propagation of individual, conspicuous features of the SSH field (e.g., Delcroix et al. 1991; Musman, 1992). However, such a "deterministic" approach permits positive identification of only rather intense events of equatorial waves, on a case-by-case basis. Altimeter measurement errors, not suppressed by averaging over a large data sample, make it difficult to resolve small-amplitude SSH oscillations (under 5 cm or so). Moreover, the plots of an "instantaneous" SSH field, based on observations over a large time interval (at least 17 days in the case of Geosat altimeter measurements and at least 10 days for Topex measurements), do not permit an accurate determination of the shape of observed waves.

The satellite data and their reduction are described in Section 2. Our statistical technique is sketched in Section 3. Section 4 reviews properties of autocorrelation functions important for our analysis. Results of the data analysis are reported in Section 5. In the Appendix we present linear model predictions for the autocorrelation function of a broad-band system of baroclinic Rossby waves. This facilitates the interpretation of the statistical quantities in Section 6. Conclusions are summarized in Section 7.

2. Dataset of SSH observations and data subletting

As described in (Benada, 1993), Topex altimeter data contain a number of standard corrections. For our application, the most important ones are the static atmospheric pressure ("inverse barometer"), electro-magnetic ("sea state") bias, tidal (solid Earth and ocean) and geoid. The residual (r.m.s.) error in SSH measurements is presentl y believed to be about 5 cm (Fu et al., 1994). In addition to the standard corrections, we introduce an orbit correction in the fashion of (Tai, 1989), as discussed in detail in (Glazman et al., 1995). Finally, we remove the time-invariant trend in the SS} I field. This is done by subtracting the mean (over the period of observations) SSH value at each spatial point from a current value, Usually this procedure is employed to eliminate remaining uncertainties in the Earth geoid. In our case, it also serves to remove spatial trends due to stationary features of ocean dynamics. Specifically, it eliminates a stationary component associated with the mean east-west slope of the sea level (caused by Trade winds) along the equator. Our check of the thus processed data showed the remaining linear trend along the equator to be 3×10^{-5} cm/km, i.e. practical] y absent. The dataset includes 530 days worth of Topex observations, covering cycles 13 through 65 - the June 93-Aug 94 period characterized by a pronounced sequence of Rossby waves.

We consider SSH spatial and temporal variations in a 12,200 km long zonal channel centered on the equator. SSH measurements are spaced roughly 6 km along the altimeter groundtracks. Figure 2 illustrates geometry of the tracks for a small area of the equatorial Pacific, based on the full (l O-day) cycle of Topex/Poseidon observations. Apparently, the minimal spatial separation of SSH measurements in the zonal direction depends on the latitude. At $\pm 2^0$ off the equator the longitudinal separation is down to about 10 km. However, on the equator this distance exceeds 150 km. This factor, along with some additional requirements described in the next section, constrains the spatial resolution of our analysis.

Altimeter data from all ascending and descending passes were. grouped into one-dimensional zonal strings spaced by about 5 km in the meridional, i.e., y - direction, Fig. 2. To estimate spatial-temporal autocorrelation function $W(r,\tau)$ at a given latitude, we employed four adjacent zonal strings. The autocorrelation functions calculated for strings in a group were ultimately averaged - to increase the statistical significance of the $W(r,\tau)$ estimation - and the mean $W(r,\tau)$ was referenced to the central latitude of a 4- strings group. Therefore, our spatial-temporal autocorrelation function represents a meridional average over a zonal "sub-channel" about 20 km wide. The analysis presented in the following sections employs four strings centered at about 0.75°S. The shape of the autocorrelation function estimated for other strings was essentially the same.

3. Evaluation of spatial-temporal autocorrelation functions and power spectra

Accurate wavenumber-frequency spectra $\Phi(\omega,k)$ would be most useful for analysis of wave processes. However, practical estimation of $\Phi(\omega,k)$ requires data on a regular space-time grid. The actual format of satellite altimeter data is not suited for the task, and interpolating the SSH data onto a regular grid would drastically degrade the spatial and temporal resolution of spectral analysis. Autocorrelation functions $W(r,\tau)$ provide an effective alternative, for they are much easier to estimate based on non-gridded data. Their use for analysis of wave processes is explained in the. next section,

For each zonal string, the data were analyzed in the following manner. In order to estimate spatial-temporal autocorrelation function $W(r,\tau)$, wc calculated SSH products $\eta(x,t)\eta(x+r,t+\tau)$ for all possible pairs of points on the (x,t) plane and grouped them by values of spatial and temporal lags into $(\Delta r, \Delta\tau)$ bins on the (r,τ) plane. Therefore, the absolute times and longitudinal positions of individual measurements were "forgotten." Strictly speaking, this is justified only for a statistically stationary and spatially homogeneous random function $\eta(x,t)$. The assumption of spatial statistical homogeneity

and stationarity implicit in our analysis is quite common in ocean and atmosphere studies. However, possible effects of non-stationarity remain largely unknown, hence the results should be treated with some caution.

The minimal size Ar of the spatial-lag bins is constrained by the longitudinal separation of satellite tracks. We selected Ar = 350 km as the optimal size. '1 'he choice of $\Delta\tau$ is based on the following compromise. On the one hand, the greater this interval, the more SSH products become available for estimating the autocorrelation function on the r-grid for a given τ. On the other hand, the distance traveled by an ocean wave during a large time interval $\Delta\tau$ may well exceed the size of the Δr-bin, hence this wave will distort the autocorrelation function. Obviously, for studies of Rossby waves, we should choose $\Delta\tau \leq \Delta r/C_R$ where CR is the characteristic phase speed of baroclinic Rossby waves ($C_R \approx 1$ m/s). Within this time interval, the surface's variations can be neglected. Therefore, $\Delta\tau$ is called the "synchronicity interval." The averaging over the time-lag bins filters out SSH oscillations with periods smaller than $2\Delta\tau$. Most of the results described in Sections 5 and 6 are obtained with $\Delta\tau$ = 4 days. Obviously, the choice of Δr = 350 km and $\Delta\tau$ = 4 days is quite adequate for analysis of baroclinic Rossby waves. However, information on gravity and Kelvin waves will be suppressed due to the averaging within the bins. Really, Kelvin waves would travel 860 km in 4 days, hence they would cross two Δr-bins. Their effect on the autocorrelation function $W(r,0)$ is illustrated later in this section.

Ultimately, all SSH products falling within the $(\Delta_1, \Delta\tau)$ cells were averaged. This yielded an unbiased estimate of the autocorrelation function $W(r,\tau)$ on the regular r-τ grid. This function characterizes the regime of SSH variations for a given period of observations. Error analysis for this technique is presented in (Glazman et al., 1995). The averaging suppresses adverse influence of altimeter measuring errors and has other advantages. The r.m.s. error of the autocorrelation function estimate, as caused by SSH measuring errors, is $\Delta_c W \approx e^2/\sqrt{N}$ where N is the mean number of independent products $\eta(x)\eta(x+r)$ in Ar bins and e is the root-mean square error of SSH measurements. For $e \approx 5$ cm and $N \approx 3 \times 10^3$, we

find $\Delta_c W \approx 0.5$ cm^2. The distribution of the number, N(r), of SSH products falling into Ar bins is presented in Fig. 3 for $\tau=0$, for several values of $\Delta\tau$. The fact that this distribution is highly non-uniform complicates estimation of error bars. However, if the lowest values of N(r) are of order 1@, the overall accuracy of the statistical analysis is sufficient to resolve 1 cm SSH variations. A more detailed description of our statistical approach is provided in (Glazman et al., 1995).

Figure 4 illustrates the effect of the synchronicity interval on the spatial autocorrelation function W(r), for a full-length zonal sub-channel centered at y = 0.75%. The diamond represents the total variance of SSH, $\langle\eta^2\rangle = W(0)$, for which both temporal and spatial lags are exactly zero. The points connected by the solid curve have the synchronicity interval ranging from 2 to 10 days (panels A through I), and the actual time difference in individual SSH products is always greater than zero: point $\langle\eta^2\rangle$ is not included into the curve (and is also ignored in the following discussion) because this point is dominated by a delta-con-elated (i.e., "white") noise due to instrumental and measuring errors.

On a close examination of panels C and D in Fig, 4, one can notice a slight eastward displacement (about 600 km in Panel C) of the peak of W(r). We explain this shift by the influence of baroclinic Kelvin waves. Really, with a 7-day synchronicity interval, Kelvin waves will make their largest positive contribution to W(r) at spatial lags $r \approx c_K t$ where $0< t <7$ days and c_K is the Kelvin phase speed. Consider a Kelvin-wave-induced component, $W_K(r)$, of the total autocorrelation function W(r). Effect of the synchronicity interval, T, is found by averaging the true spatial-temporal autocorrelation function, $K(r,\tau)$, of Kelvin waves over all time-lags within T:

$$W_K(r) = \frac{1}{T}\int_0^T K(r - c_K\tau)d\tau = \frac{1}{cT}\int_{-c_K T/2}^{c_K T/2} K(\rho - \xi)d\xi$$

Here we introduced $\xi = c_K\tau - c_K T/2$ and $p = r - c_K T/2$. As a function of p, this autocorrelation function is even: $W_K(\rho) = W_K(-\rho)$, which yields $r_m = c_K T/2$ for the point at which $W_K(r)$ attains its maximum. With T = 7 days and c_K = 2.5 m/s, $r_m \approx$ 750 km.

The dominance of the Kelvin-wave-induced component of W at these small time scales explains why this r_m is in a reasonable agreement with Fig. 4(C).

The spatial autocorrelation function, Fig. 4, shows a near-linear behavior at large scales -- from about 1000 to 9000 km. The corresponding shape of the wavenumber spectrum is inferred based on the following argument. The 1 d wavenumber spectrum of form

$$F(k) \propto k^{-3+2\mu} , \tag{1}$$

with $\mu > 0$, yields the following asymptotic form of the spatial autocorrelation function:

$$W(r) \approx W(0) - Br^{2-2\mu} , \tag{2}$$

(e.g., (Glazman and Weichman, 1989)). Here, B is a constant. Hence, when W(r) is a linear function ($\mu = 1/2$), the spectrum follows power law $F(k) \sim k^{-2}$ in the corresponding range of wavenumbers.

The spatial-temporal autocorrelation function is illustrated in Fig. 5.

In principle, autocorrelation functions permit estimation of power spectra. However, random errors in the values of $W(r,\tau)$ and the limited] ange of r and τ for which $W(r,\tau)$ is estimated would greatly degrade the accuracy of the corresponding Fourier transform. Therefore, the direct use of autocorrelation functions for analyzes of wave properties is preferable.

4. Using autocorrelation functions for analysis of wave processes

The spatial-temporal autocorrelation funct ion, Fig, 5, contains a great deal of information on processes occuring within our 530-day period of observations. For example, let us notice that the secondary ridge of $W(r,\tau)$ is separated from the main one by $\tau \approx 1$ year. This ridge (and its mirror image at negative τ) is associated with the inter-annual variability rather than the intrinsic period of Rossby waves. Most relevant to our problem is the main ridge of $W(r,\tau)$, especially the part for which the lag is well within 100 days -- the time required for long baroclinic Rossby waves to freely traverse the equatorial channel at

the sped ≈ 1 m/s. For this range of τ, $W(r,\tau)$ is related to the wavenumber spectrum of SSH zonal variations by

$$W(r,\tau) = \int F(k) e^{ik[r-c(k)\tau]} dk \ , \tag{3}$$

where c(k) is the wave phase velocity. For a narrow-band spectrum F(k), the integral can be evaluated by the stationary phase method. This would immediately demonstrate that the most prominent feature of the 2-dimensional function $W(r,\tau)$ is a "ridge" on the r-τ plane passing through the origin. Its orientation yields the propagation speed of a wave train, $d\omega/dk$. The latter, of course, is the wave group velocity. (Provided the spectrum is sufficiently narrow, a system of parallel ridges of a rapidly decreasing height would also be visible on this plane.) In a non-dispersive case (c(k) is const), (3) reduces to

$$W(r,\tau) = W(r - c\tau) \tag{4}$$

In other words, $W(r,\tau)$ at time τ is obtained from $W(r,0)$ by a uniform shift along r. The wave propagation speed, c, is found as

$$c = \frac{r(\tau)}{\tau} \tag{5}$$

Here, $r(\tau)$ is the position of the correlation maximum at time τ. Obviously, equation (4) remains also valid in the case of wave solitons because wave dispersion is exactly balanced by effects of wave non-linearity: the wave shape travels without distortions.

For a broad-band spectrum, such as (1) with $\mu > 0$, the interpretation of the autocorrelation function is not trivial. In the Appendix, we carry out numerical simulations of $W(r,\tau)$ for a special case of linear Rossby waves whose spectrum contains a power-law range k^{-2}.

5. Statistical analysis of baroclinic Rossby waves

a) Spatial autocorrelation function and wavenumber spectrum

Figures 4 and 5 point to the existence of two regimes of SSH spatial variations. The short-scale variations responsible for a narrow peak at the origin have spatial scales under 1000 km and are characterized by SSH variance $\langle\eta^2\rangle \approx 16$ cm2 estimated as $W(0)$-$W(\Lambda)$

where A is the characteristic spatial lag (A ≈ 10^3 km) at which W(r) starts displaying the linear trend, and W(0) is presented in Fig. 4 by a dian ıond. The long-range variations (corresponding to the linear trend in W(r)) have spatial scales greater than about 1000 km, Their variance, $\langle\eta^2\rangle \approx 8\ cm^2$, is found as W(A). A more formal evaluation of the SSH variance for large spatial scales can be done by fitting a parabola $a_0 - a_2 r^2$ to several points with $|r| > 1000$ km surrounding the W(r)'s narrow peak: its maximum, a_0, provides the desired result.

In accord with(1) and (2), the linear behavior of W(r) on scales from about 1000 km and to almost the basin size scale corresponds to the k‘2 range in the 1-d power spectrum F(k). The power spectrum pertaining to these large-scale oscillations can be idealized as

$$F(k) = const \cdot e^{-(k_0/k)^2} e^{-(k/k_\infty)^2} k^{-2} \qquad (6)$$

where the exponential factors serve as the high- and low-pass filters, respectively: k_0 representing the lower-wavenumber boundary of the linear range and k_∞ serving as the "microscale" or the “inner scale” of the spectrum [see, e.g., (Glazman and Weichman, 1990) for a discussion of this kind of spectra]. The use of a low-pass filter is necessary only for the study of the SSH profile (reported in section 6) to guarantee convergence of an improper integral. To better understand the narrow peak of W(r) corresponding to small-scale motions one has to analyze the temporal evolution of $W(r,\tau)$.

b) Spatial-temporal autocorrelation function

Figure 6 illustrates several sections of $W(r,\tau)$ for fixed values of the temporal lag. Ignoring for a moment the evolution of $W(r,\tau)$ near its peak, we earl estimate the speed of the westward propagation using (5). Based on the last three panels in Fig. 6- with τ = 40, 60 and 80 days -we find $\bar{c} \approx 1.1$ m/s - in agreement with previously known estimates for baroclinic Rossby waves, see e.g. (Delcroix et al., 1991) and references therein.

A more formal estimation of this speed can be done, for instance, as follows. For each fixed value of τ, one can estimate the r-coordinate of the autocorrelation maximum and then fit a straight line $r(\tau)=c\tau$ to all such points within a selected range of z-values. The

autocorrelation maximum for a fixed τ is found by approximating $W(r;\tau)$ by a quadratic polynomial $a_0+a_1r+a_2r^2$ and solving equation $\partial W/\partial r = 0 = a_1+2a_2r$ for r. With step $\Delta\tau$ = 4 days (for values of τ from 20 to 80 days), this procedure yields c ≈ 1.11±0.22 m/s where the uncertainty of 0.22 m/s is taken as the standard deviation of experimental points from the straight line $r(\tau) = \bar{c}\,\tau$. Since the total number of such points is n = (80-20)/4 =15, we estimate confidence intervals as $\Delta c = t\,\sigma/\sqrt{n}$ where σ is the standard deviation, σ = 0.22 m/s, and t is found from Table 26.10 of (Abramowitz and Stegun, 1970) for a specified value of the significance level, A. Taking A = 0.9, we find Δc = 0.1 m/s. Therefore, at the 90 percent significance level, we have c = 1.11 ± ().10 m/s,

If the wavenumber spectrum were narrow, $\bar{c}$ could be viewed as the wave group velocity of baroclinic Rossby waves corresponding to the spectral peak wavenumber. In our case, $\bar{c}$ strongly depends on the spectrum shape. Hence, its usefulness as a characteristic of the equatorial waveguide is not very high. In this respect, the Kelvin wave speed represents a more fundamental quantity, for Kelvin waves arc non-dispersive and their velocity is determined by the Brunt-Väisälä frequency. A detailed analysis of this issue is presented in the next section,

As evident from Figs. 4 through 6, the sharp peak in $W(r,\tau)$ is confined to the shortest temporal and spatial scales. These short-scale variations may be caused by the following factors:

1) SSH measuring errors, such as the electromagnetic (sea state) bias caused by wind-generated surface gravity waves. With respect to the coarse spatial and temporal resolution of the our technique, this factor represents a delta-correlated noise, hence it contributes only to $W(0,0)$.

2) High-frequency SSH oscillations due to barotropic and fastest baroclinic gravity wave modes. Considering the relatively large size of the time-lag bins, $\Delta\tau$, contribution of these fast waves is similar to that of a delta-correlated noise: they increase $W(r,\tau)$ only for smallest values of τ.

3) Kelvin waves. Similar to other high-frequency oscillations, Kelvin waves - due to their short wave period (2.4 days for a 500 km wavelength) - would require a very small synchronicity interval for their detection. Although these waves are not observed in Figs. 5-6 (because of the large lag bins used in our analysis), they manifest themselves in the eastward shift of the W(r) peak in Fig. 4 panels C and D.

4) Short Rossby waves. These are defined as the waves with wavelengths shorter than the Rossby radius of deformation. Considering the relatively large size of the spatial-lag bins, Ar, effect of short (although slow) Rossby waves is similar to that of fast waves, except that these waves would manifest themselves as spatial rather than temporal delta-correlated noise. Therefore, they could increase $W(r,\tau)$ only at short spatial lags r.

For our analysis of long baroclinic Rossby waves, all these processes present little interest.

6. Interpretation of the results

Since we have no information on higher statistical moments, the interpretation of Figs. 4-6 depends on our assumptions regarding the phase coupling between Fourier components comprising the spectrum. The simplest assumption is that the SSH variations represent a Gaussian random field. In particular, there is no phase coupling between individual Fourier components - the waves are linear. In the Appendix, a linear-wave analysis is presented to relate the propagation speed, $\bar{c}$, of the autocorrelation maximum, which was estimated based on our SSH data, to the phase speed, $c_{R,1}(0)$, of longest (non-dispersive) baroclinic Rossby waves. In this section we show, in particular, that the observed $\bar{c}$ is higher than predicted by linear theory. This and other arguments presented in this section lead us to suggest that the linear theory of baroclinic Rossby waves is at odds with our observations.

Most of the earlier experimental studies reported the value of the Kelvin wave speed, c_K, rather than the Rossby wave speed, Indeed, c_K is a convenient intrinsic property of

the equatorial waveguide because it is unambiguously related to the Brunt-Väisälä frequency. In order to express our experimental quantity $\bar{c}$ in terms of the Kelvin speed, we need the following theoretical relationship between c_K and the phase speed, $c_{R,m}(0)$, of the longest Rossby waves of the m-th meridional mode (e.g., LeBlond and Mysak, 1978):

$$c_K = -(2m+1)c_{R,m}(0), \qquad (7)$$

where $c_{R,m}(k)$ is the phase speed of the m-th Rossby mode for wavenumber k. Equation (A8) shows that $c_{R,m}(0)$ must be about 1.15 times as high as the propagation speed of the autocorrelation maximum. Using $\bar{c} \approx 1.1$ m/s this yields $c_{R,m}(0) = 1.2$ m/s. According to (7), our measured $\bar{c}$ would correspond to the Kelvin speed of 3.6 m/s. This value is well outside the range of typical Kelvin speeds (2.3 to 2,8 m/s) reported for the equatorial Pacific.

The hybrid, Rossby-gravity mode, m=O, (also known as the Yanai wave) does not agree with our observations, either. As shown in the Appendix, this mode is inconsistent with the shape of $W(r,\tau)$. in Fig. 6.

Of course, one may try explaining the high value of $c_{R,1}(0)$ by possible inaccuracies of our data analysis. However, we believe that a more relevant explanation can be suggested based on non-linear theories of equatorially - trapped waves.

A non-linear theory of Rossby waves due to Boyd (1980) yields a single-hump soliton or a modon [provided the amplitude is above a certain threshold (Boyd, 1985)] propagating at the speed that exceeds $c_{R,m}$ by an amount proportional to the wave amplitude. Let us show that a soliton gas hypothesis is consistent with the observed autocorrelation function of SSH variations. As evident from Fig. 6, the peak value of $W(r,\tau)$ established at $\tau \approx 20$ days does not drop as the time lag continues to increase, whereas the linear theory predicts a monotonic decrease of the $W(r,\tau)$ peak value with an increasing τ, Fig. 8. For dispersive waves this can happen only if the effect of wave dispersion is counteracted by the effect of wave non-linearity, as is the case for Rossby solitons.

The other argument in support of the soliton gas hypothesis is that the longest waves in the spectrum, being near the basin length size, would be affected by the western boundary which would prevent their propagation as either free or forced progressive waves. However, as the Fourier components of a compact, soliton-like formation, these waves cause no controversy. The surface profile of a non-Gaussian random field with power spectrum (6) can be constructed based on the following idealization. Let the instantaneous wave field $\eta(x;t)$ be comprised of (identical) surface disturbances, η_n:

$$\eta(x) = \sum_n \eta_n(x - x_n), \tag{8}$$

satisfying condition η_n (x) $\rightarrow$ O at I xl $\geq L$ where L characterizes the width of a soliton. In other words, individual solitons are well separated in space. If, additionally, the spacing is constant, a Fourier transform, f(k), of the surface profile is given by the Fourier transform of a single soliton times a constant which is inversely proportional to the number of solitons per unit length of the surface. Obviously, this Fourier transform is related to the power spectrum (6) by F(k) $\propto$ [f(k)]^2. Therefore, the surface profile is found as the real part of $(2\pi)^{-1}\int_{-\infty}^{\infty}[F(k)]^{1/2}e^{-ikx}dk$. This profile is illustrated in Fig. 7. Unfortunately, in the small vicinity of its peak, the shape of this "soliton" is strongly affected by our choice of the low-pass filter in (6). Not knowing the "amplitude" (in terms of the thermocline depth displacement) of these disturbances, we cannot indicate their theoretical propagation speed However, the fact that this speed would exceed the phase sped of linear Rossby waves indicates that a Rossby soliton (or its higher-nonlinear version - the modon) is consistent with our observations.

The theoretical shape of Rossby solitons (Boyd, 1980) is different from that in Fig. 7. However, since the spacing and amplitude of individual solitons are not constant, the above analysis should not be viewed literary as a derivation of the mean shape. This shape also depends on statistical distributions of quantities entering (8). Our main goal here was only to show that a broad-band spectrum, such as k^{-2}, may lead to single-hump formations of a reasonable horizontal extent - comparable to that of Rossby solitons.

Alternative explanations arealso possible. In particular, one could suggest that the observed F(k) spectrum is the result of weak wave turbulence. Unfortunately, theoretical spectra for this case are absent, because present theories of Rossby wave turbulence are limited to short (as compared to the Rossby radius of deformation) waves (e.g., Zakharov et al., 1992).

6. Summary and conclusions

Equatorially-trapped waves represent a rich dynamical system characterized by many degrees of freedom. Statistical analysis of ocean wave observations, as opposed to a determination of individual wave properties on a case by case basis, offers a natural way of studying such systems. This is especially true for satellite-altimeter data because their temporal and spatial resolution and measuring accuracy are limited while the spatial and temporal coverage is quite large. The technique employed in the present work allowed us to infer some new and interesting properties of baroclinic Rossby waves.

Our main finding is that, in a wide range of scales (from about 10^3 to 10^4 km), zonal spectra of equatorial Rossby waves exhibit a power-law behavior $F(k) \sim k^{-2}$. Present interpretation of these waves as a sequence or baroclinic Rossby solitons is tentative, for we have no information on higher statistical moments of the wave field. Such information is necessary in order to directly assess the degree of the phase coupling between Fourier components. The main arguments in support of the soliton gas hypothesis are summarized as follows:

1) At sufficiently large values of time lag, 20 days $\leq \tau_c$ 80 days, our function $W(r,\tau)$ preserves its shape as τ continues to increase, see Fig, 6. (The upper bound on τ represents the time taken by a signal to pass $8 \cdot 10^3$ km at speed 1.2 m/s.) We interpret this observation as an indication that wave dispersion is balanced by wave non-linearity - as expected of a collection of solitons.

2) The observed propagation speed, $\bar{c} \approx 1.1$ m/s, appears to be higher than the prediction of linear theory.

3) A power-law spectrum k^{-2} of westward propagating waves with length scales up to $8 \cdot 10^3$ km - comparable to the basin size - corresponds to a set of compact, soliton-type, formations.

In the absence of higher-order statistical moments we cannot eliminate a possibility of weak wave turbulence as being responsible for the observed spectrum, However, at the present time, estimation of bispectra or other characteristics of a non-Gaussian random field of SSH variations is impeded by the relatively low measuring accuracy, limited spatial and temporal resolution and still insufficient volume of SSH observations. The use of alternative statistical approaches might prove advantageous in future studies.

APPENDIX A: Linear model of Rossby and Yanai waves

Linear theory yields the following dispersion relationship for the 1st meridional mode Rossby waves:

$$\omega = -\frac{kc_K}{\beta + 2(kR)^2}, \qquad \text{(A1)}$$

where c_K is the Kelvin wave speed, $c_K \equiv \sqrt{g'h} \approx 2.5$ m/s, and

$$R = \left(\frac{\sqrt{g'h}}{2\beta}\right)^{1/2} \qquad \text{(A2)}$$

is the internal Rossby radius of deformation, and $\beta \approx 2.3 \cdot 10^{-11}$ (m s)$^{-1}$. In the case of a two-layered ocean, g' is the reduced gravity and $h = H_1 H_2 / (H_1 + H_2)$ where H_1 is the thermocline depth and H_1+H_2 is the total ocean depth, H. For the first vertical mode in a continuously stratified ocean, h in (A2) is replaced with $(NH/\pi)^2/g$ where N is the Brunt-Väisälä frequency, and g' is replaced with g. We are concerned with the case when the Rossby radius is small - as specified later in this section. For brevity, let us re-denote the Rossby wave phase speed $c_{R,m}(k)$ by $c(k)$ and $c_{R,m}(0)$ by c_0. For long Rossby waves,

the dispersion relationship can be simplified by assuming $(Rk)^2 << m+1/2$ fork in the range (k_0, k_∞). Thus, the phase speed is

$$c(k) \approx c_0(1 - \varepsilon k^2) , \tag{A3}$$

where

$$c_0 = -\frac{\sqrt{g'h}}{2m+1} , \qquad \varepsilon = \frac{R^2}{m+1/2} \tag{A4}$$

Let us write **(3)** with **(A3) in a non-dimensional** form

$$\tilde{W}(\tilde{r},\tilde{\tau}) = \int_0^\infty \tilde{F}(\kappa)\exp[iQ\kappa(\tilde{r}-\tilde{\tau}) + i\tilde{\varepsilon}\tilde{\tau}\kappa^3]d\kappa , \tag{A5}$$

where the non-dimensional variables are related to R, c_0 and k_0 by the following scaling relationships:

$$\kappa = k/k_0, \quad \tilde{r} = r/L, \quad \tilde{\tau} = \frac{c_0}{L}\tau, \quad Q = k_0 L, \quad \tilde{\varepsilon} = \frac{(k_0 R)^2 Q}{m+\frac{1}{2}} \tag{A6}$$

Here, the spatial length scale L *is* arbitrary. Selecting $L = 5\cdot 10^3$ km, $k_0 \approx 2\pi\cdot 10^{-4}$ rad/km and c_K = 2.5 m/s, we have for $m=1$: $R \approx 233$ km, $c_0 \approx 0.83$ m/s and $\tilde{\varepsilon} \approx$ 0.04. These values of c_K and R *are* typical for the equatorial Pacific (LeBlond and Mysak, 1978). The corresponding time scale $L/c_0 \approx$ 70 days.

The non-dimensional version of(6) is

$$F(\kappa) = \exp(-1/\kappa^2)\kappa^{-2} \tag{A7}$$

(We omit the low-pass filter in (6) because the integral (A5) converges sufficiently fast.) In Fig. 8, the real part of (A5) is plotted based on numerical integration. At time moment $\tilde{\tau} = 1$ (corresponding to 70 days), the maximum of $W(r,\tau)$ is found at a point $\tilde{r}$ ==-0.87. In the absence of wave dispersion it would be at a point $\tilde{r} = -1$. This delay allows one to estimate the ratio of the longest-Rossby-wave speed to the propagation speed of the autocorrelation maximum (5):

$$c_0/\bar{c} \approx 1/0.87 \approx 1.15 . \tag{A8}$$

In order to show that the mixed Rossby-gravity mode, m=O, cannot be responsible for the observed $W(r,\tau)$, one may use the (non-dimensional) dispersion relationship for these

waves, $\tilde{\omega} = [1 + \sqrt{1 + 2 / (\nu\tilde{k})^2}\,]/2$, **in the linear model** analogous to (A5). Here, $\nu = k_0 R$. *The* result is shown in Fig, 9 (all scaling parameters as the same as for Fig, 8). Evidently, the broad-band spectrum of the Yanai wave-s is inconsistent with our estimate of the spatial-temporal autocorrelation function.

ACKNOWLEDGMENTS: This work was performed at the Jet Propulsion Laboratory, California Institute of Technology, under contract with the National Aeronautics and Space Adrninistration. The authors also thank Prof. L. Piterbarg of the Math. Dept. at USC for valuable comments.

BIBLIOGRAPHY:

Abrarnowitz, M., and I.A. Stegun, Handbook of Mathematical Functions, 1045 pp. Nat. Inst. of Standards and Technology, U.S. Department of Commerce, Gaithersburg, MD., 1970.

Benada, R., Internal Publication of the Jet Propulsion Laboratory, D-1 1007 "Merged GDR (Topex/Poseidon) Users Handbook, Version 1.", September, 1993.

Boyd, J.P. Equatorial solitary waves. Part I: Rossby solitons. Journ. Phys. Oceanogr., 10(1 1), 1699-1717, 1980.

Boyd, J.P. Equatorial solitary waves. Part 3: Westward-traveling modons. Journ. Phys. Oceanogr., 15(1), 46-54, 1985.

Delcroix T., Picaut J., and Eldin G. Equatorial Kelvin and Rossby waves evidenced in the Pacific ocean through Geosat sea level and surface. current anomalies. J. Geophys. Res., Oceans. 96, 3249-3262. 1991.

D'yachenko, A.I., V.E. Zakharov, A.N. Pushkarev, V.F. Shvets, and V.V. Yan'kov. Soliton turbulence in non-integrable wave systems. Sov. Phys. JETP 69(6), 144-1147, 1989.

Fu, L.L, E.J. Christensen, C.A. Yamarone Jr., M, Lefebvre, Y. Menard, M, Dorrer, and P. Escudier. TOPEX/POSEIDON mission overview. J. Geophys. Res., 99(C12), 24,369-24,381, 1994.

Glazman, R.E., A. Fabrikant, and A. Greysukh. Statistics of spatial-temporal variations of sea surface height based on Topex altimeter measurements. Int. J. Remote Sensing. (In review).

Glazman, R.E., and P. Weichman. Statistical geometry of a small surface patch in a developed sea. J. Geophys. Res., 94(C4), 4998-5010, 1989.

Kingsep, A. S., L.I. Rudakov, and R.N. Sudan. Phys. Rev. Lett. 31, 1482, 1973.

LeBlond, P.H. and L.A. Mysak. Waves In The Ocean. Elsivier, New York, 1978,602 pp.

Marshall, H.G. and J.P. Boyd. Solitons in a continuous stratified equatorial ocean. Journ. Phys. Oceanogr., 17(7), 1016-1031, 1987.

Musman, S., 1992, Geosat altimeter observations of long waves in the equatorial Atlantic. J. Geophys. Res., 97(C3), 3537-3579.

Tai, C.-K. , Accuracy assessment of widely used orbit *error* approximations in satellite altimetry and its oceanographic implications, J.Atm Oceanic Techn., 6, 147-150, 1989.

Captions for Figures

Figure 1. Period of linear baroclinic Kelvin and Rossby waves (1st baroclinic, 1st meridional mode) versus wavelength, based on equation (A 1). The Kelvin wave speed is assumed to be 2.5 m/s and the (1st baroclinic) Rossby radius of deformation 250 km.

Figure 2, Satellite ground tracks in a tropical Pacific region during a 10-day cycle, A horizontal dotted line illustrates the position of a zonal string: the SSH data are sampled from groundtracks at intersections with the string.

Figure 3. Number N(r) of SSH products falling into 350 km r-bins for W(r,0) of the full-length zonal string. Values of the synchronicity interval are provided on top of each panel.

Figure 4. One-dimensional spatial autocorrelation function, W(r), for the area 160^0 - 270^0W referenced to latitudinal position y = 0.75%, estimated for several values of the synchronicity interval At, as indicated on top of each panel. The diamond represents $W(0) \equiv \langle\eta^2\rangle$. The solid curve approximating W(r) ignores this special point because this is the only point for which both r and τ are exactly zero (see Sections 3 and 5 for detail).

Figure 5. Spatial-temporal autocorrelation coefficient, $W(r,\tau)/W(0,0)$, fOr y = 0.75°S, calculated for y = 0.5^0S. Here, W(0,0) = 24 cm2 ($\equiv \langle\eta^2\rangle$). Bold contours correspond to $W(r,\tau)=0$.

Figure 6. Spatial-temporal autocorrelation function, $W(r,\tau)$, for y = 0.75°S, for selected time lags, τ , as designated on top of each panel. Horizontal axis: r (km). Vertical axis: $W(r,\tau)$ (m^2). Synchronicity interval At=4 days.

Figure 7. Non-dimensional surface profile, $\tilde{\eta}(\tilde{x})$, for spectrum (6) with k_0 /km= 0.1. Sea surface is assumed to be a sequence, (8), of single-hump disturbances (the "soliton gas"). Vertical axis: arbitrary units of nondimensional length. Horizontal axis is scaled as $\tilde{x} = xk_0$ where x is the dimensional distance along the equator and k_0 is the low-wavenumber cutoff introduced in (6). Therefore, $\tilde{x}$ = 1 corresponds to x=1500 km. Inset: the expanded region in the vicinity of $\tilde{x}$=0.

Figure 8. The non-dimensional spatial-temporal autocorrelation function (A5) (normalized to unity at r=0) for linear Rossby waves with spectrum (A7). Horizontal axis: the non-dimensional spatial lag, $\tilde{r}$, (scaledbyL=5'10? km). Other scales are. indicated in the Appendix. Numbers at the curves are values of $\tilde{\tau}$ with time scale $1/c_0 \approx$ 70 days. Dashed curve: $\tilde{\tau}$=0.

Figure 9. The same as Fig.8, but for linear Yanai waves with v = 0.14. Numbers at the curves are values of $\tilde{\tau}$. The curve for $\tilde{\tau}$=0 is not plotted - as it is identical to the dashed curve in Fig. 8.

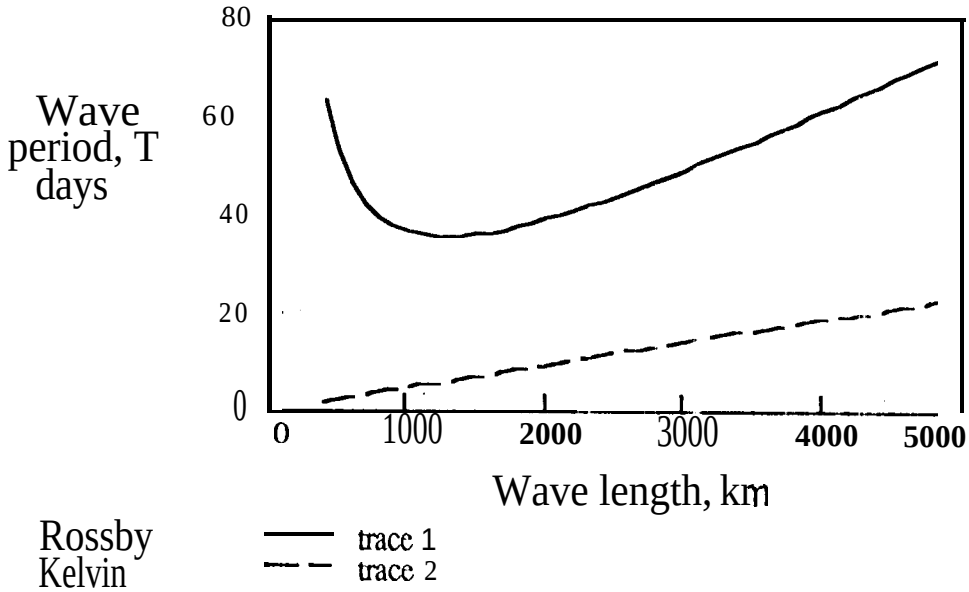
Wave period, T days
80
60
40
20
0
0
1000
2000
3000
4000
5000
Wave length, km
Rossby
Kelvin
trace 1
trace 2

Fig. 1.

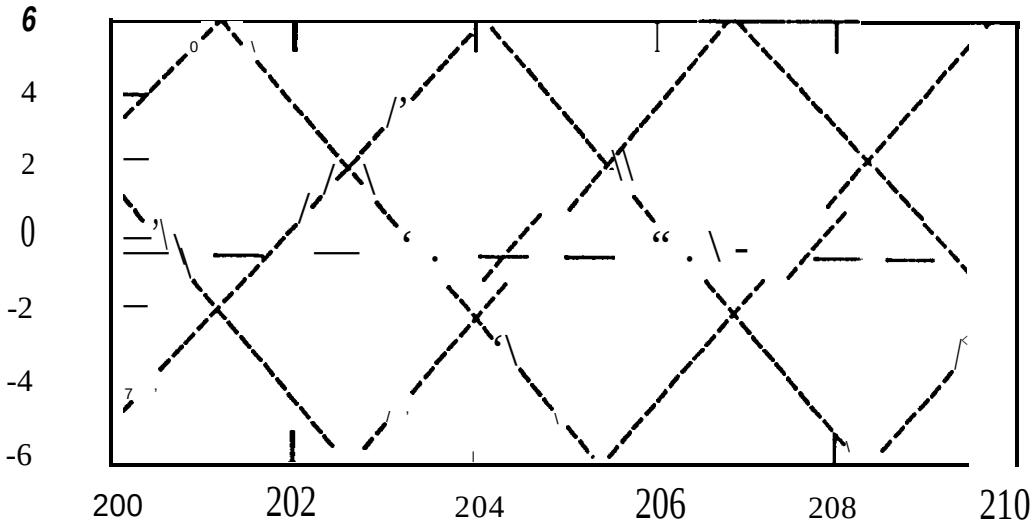

Fig. 2

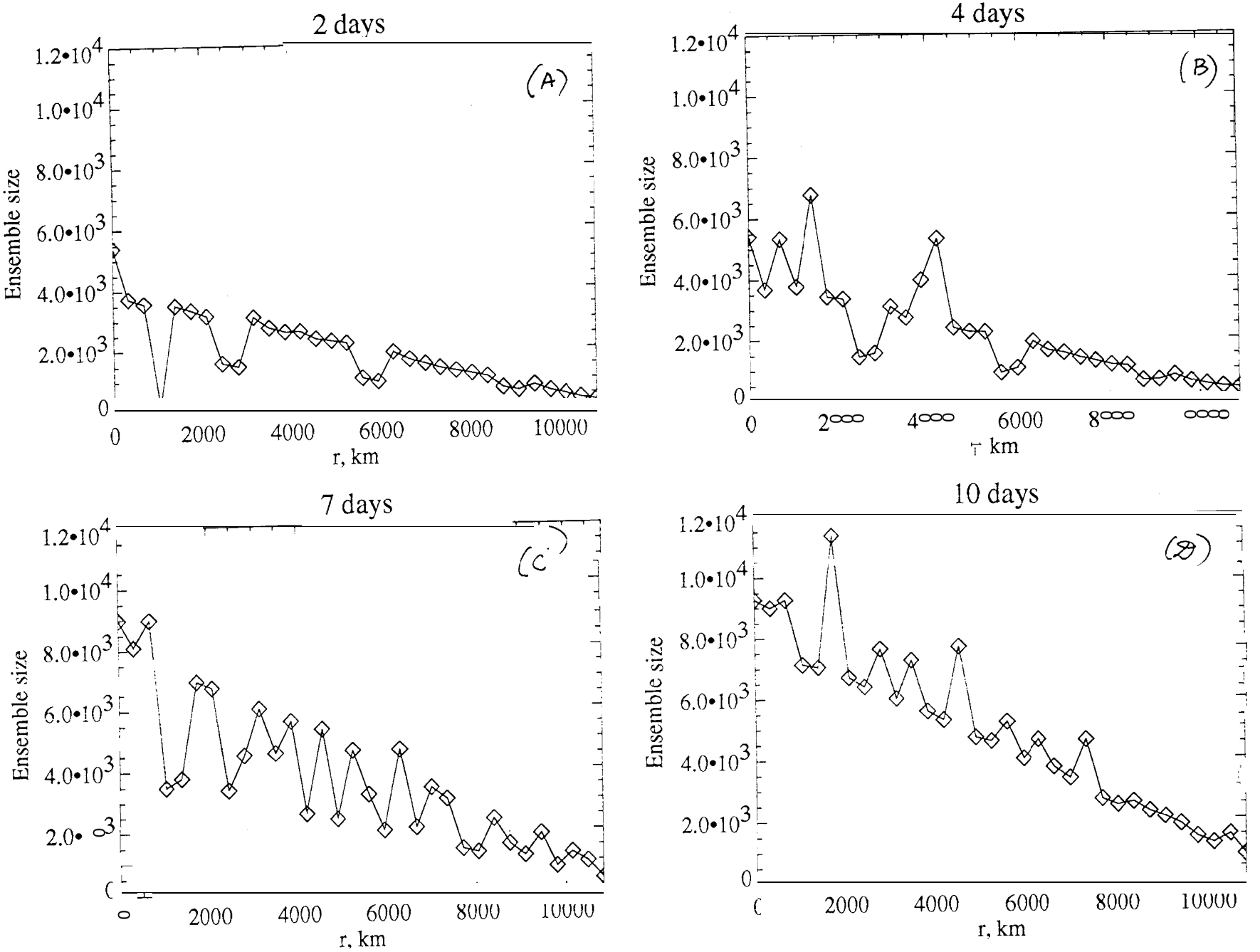
2 days
(A)
Ensemble size
1.2•10^4
1.0•10^4
8.0•10^3
6.0•10^3
4.0•10^3
2.0•10^3
0
0
2000
4000
6000
8000
10000
r, km
4 days
(B)
Ensemble size
1.2•10^4
1.0•10^4
8.0•10^3
6.0•10^3
4.0•10^3
2.0•10^3
0
0
2000
4000
6000
8000
r, km
7 days
(C)
Ensemble size
1.2•10^4
1.0•10^4
8.0•10^3
6.0•10^3
4.0•10^3
2.0•10^3
0
0
2000
4000
6000
8000
10000
r, km
10 days
(D)
Ensemble size
1.2•10^4
1.0•10^4
8.0•10^3
6.0•10^3
4.0•10^3
2.0•10^3
0
0
2000
4000
6000
8000
10000
r, km

Fig. 3

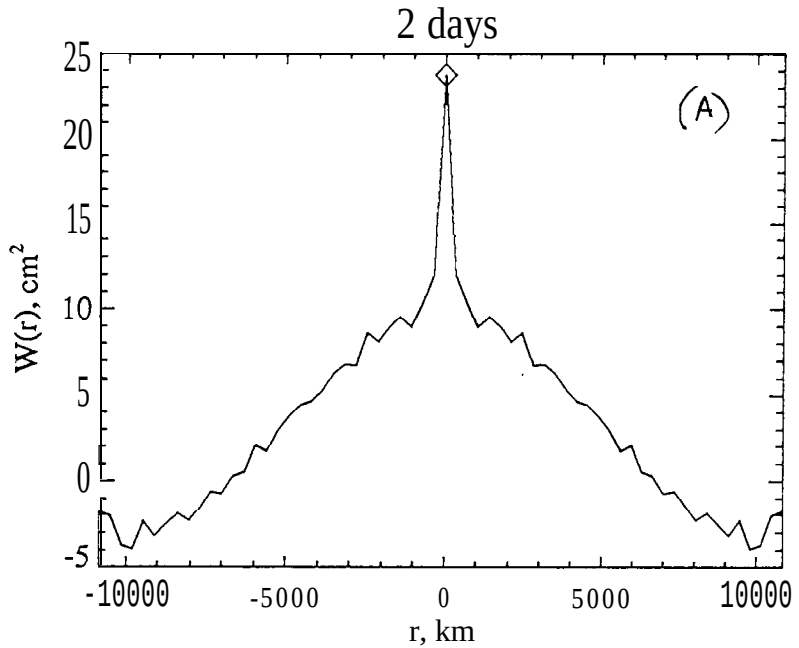
2 days
(A)
W(r), cm^2
r, km
25
20
15
10
5
0
-5
-10000
-5000
0
5000
10000

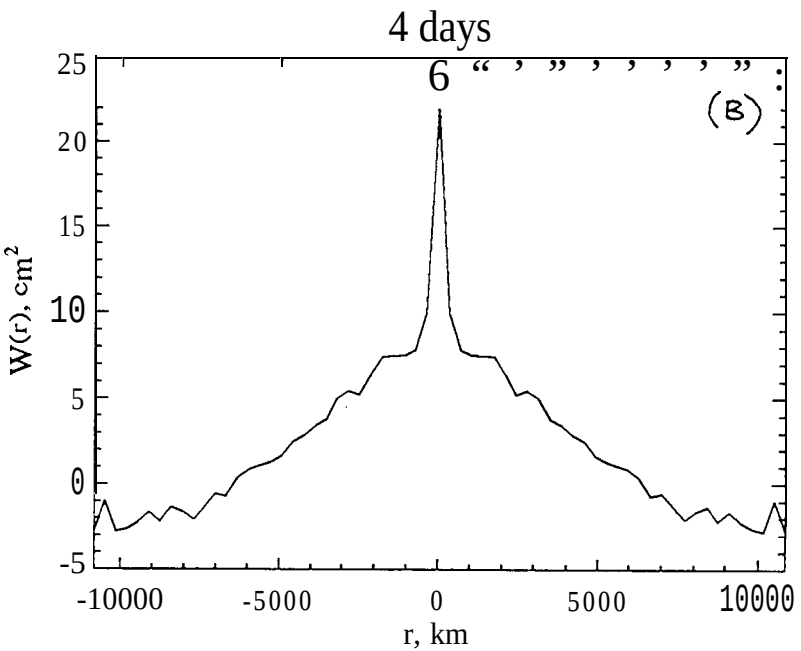
4 days
(B)
W(r), cm^2
r, km
25
20
15
10
5
0
-5
-10000
-5000
0
5000
10000

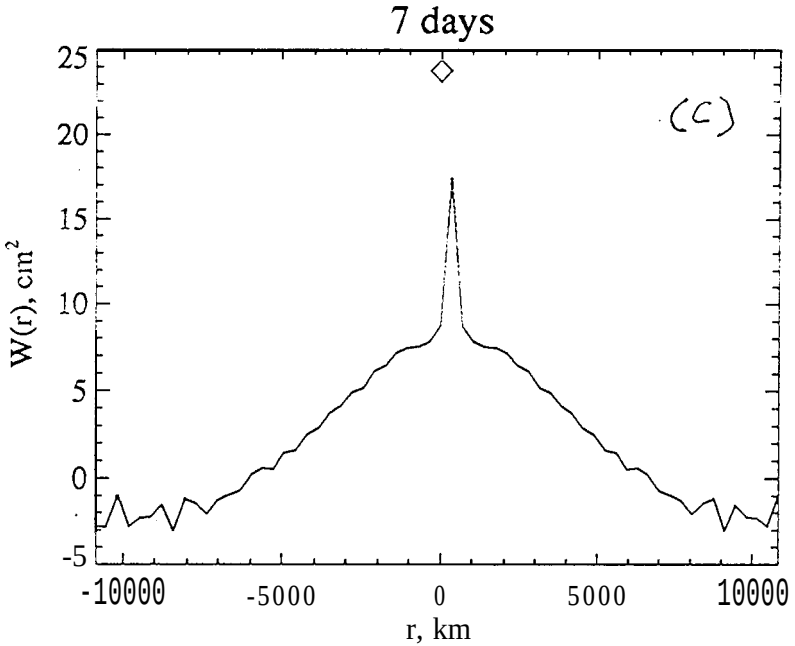
7 days
(C)
W(r), cm^2
r, km
25
20
15
10
5
0
-5
-10000
-5000
0
5000
10000

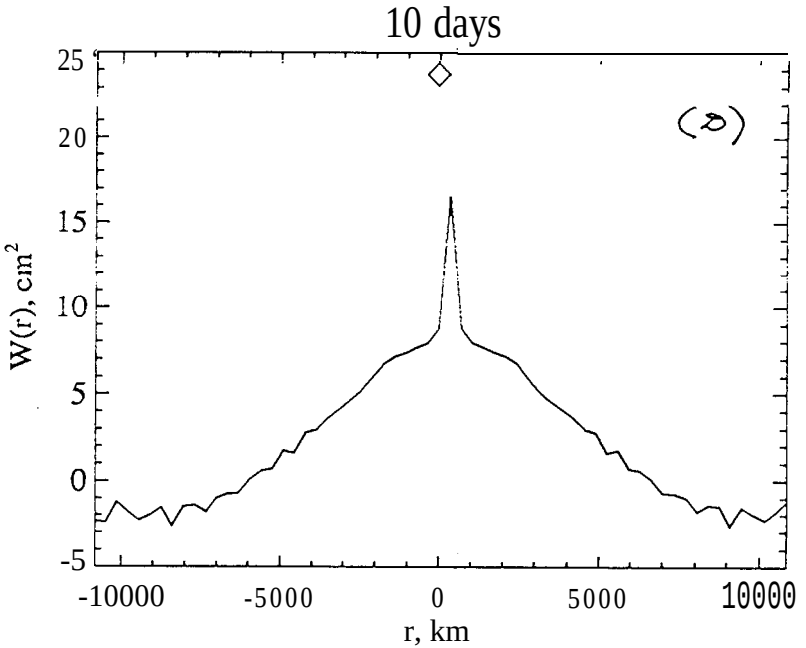
10 days
(D)
W(r), cm^2
r, km
25
20
15
10
5
0
-5
-10000
-5000
0
5000
10000

Fig. 4

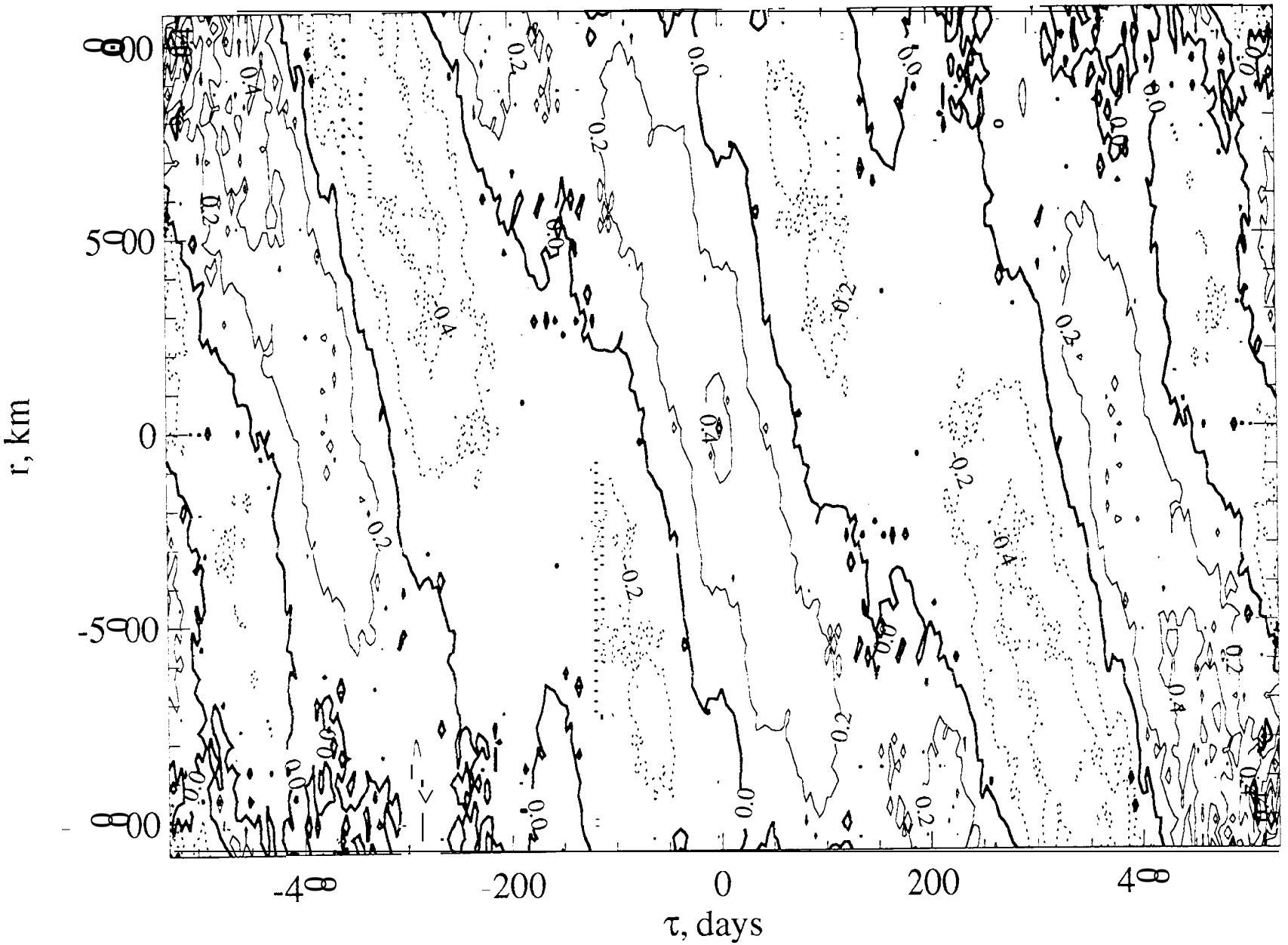

Fig 5

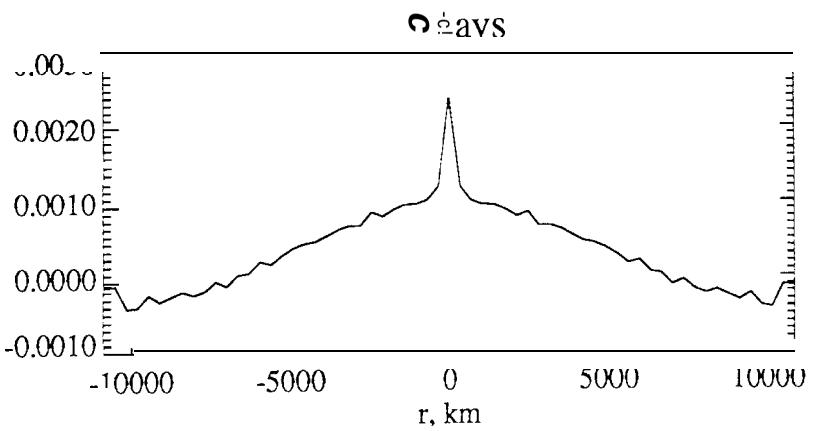
0.0020
0.0010
0.0000
-0.0010
-10000
-5000
0
5000
10000
r, km

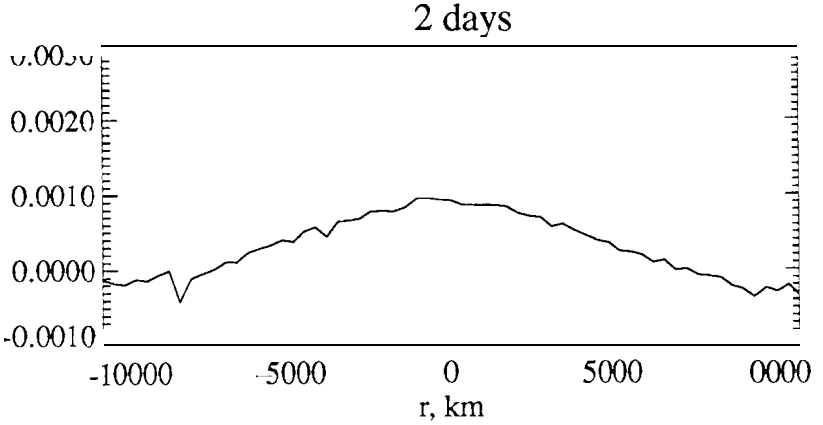
2 days
0.0020
0.0010
0.0000
-0.0010
-10000
-5000
0
5000
r, km

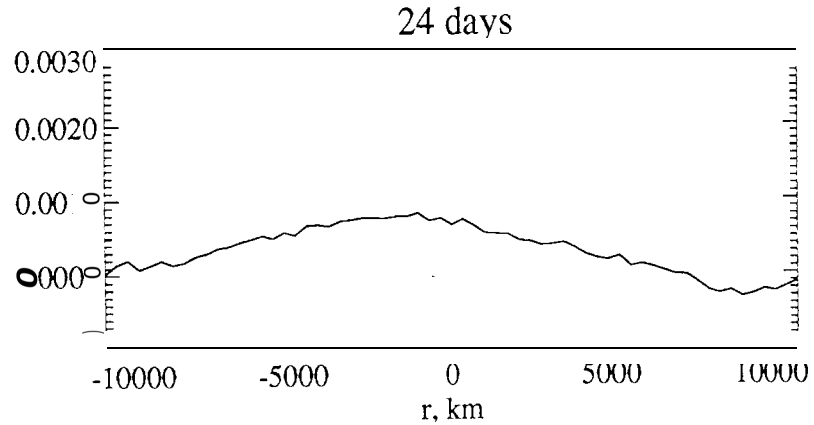
24 days
0.0030
0.0020
-10000
-5000
0
5000
10000
r, km

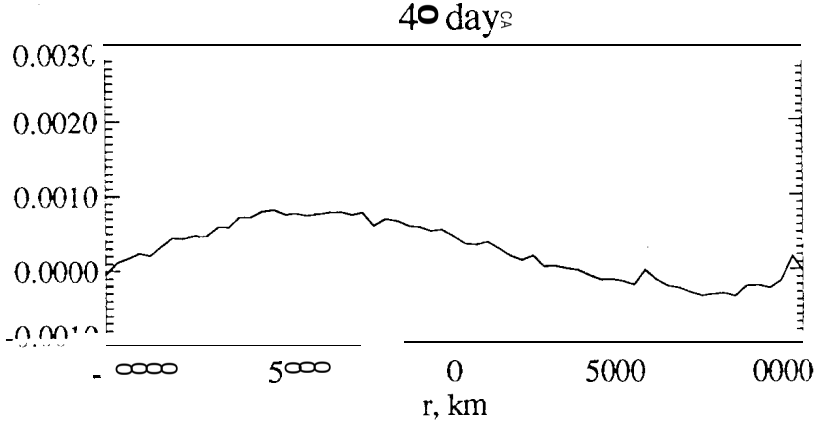
0.0020
0.0010
0.0000
5000
0
5000
r, km

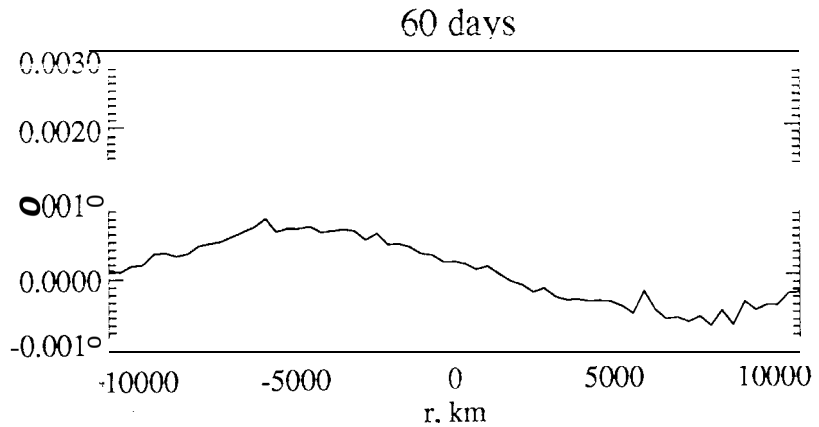
60 days
0.0020
0.0000
-10000
-5000
0
5000
10000
r, km

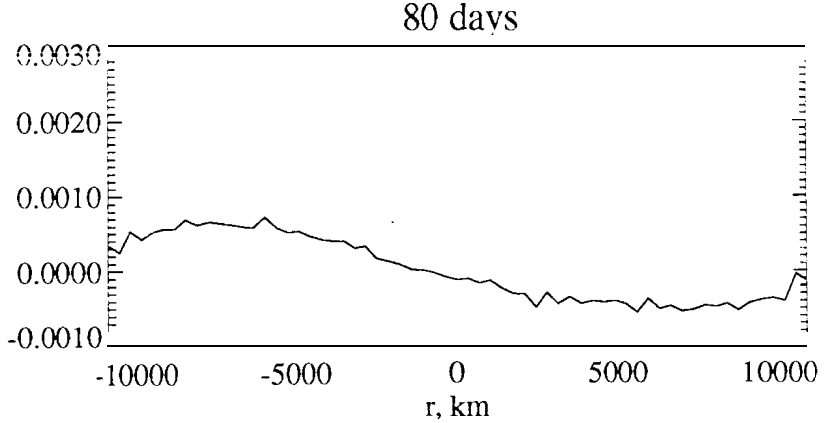
80 days
0.0030
0.0020
0.0010
0.0000
-0.0010
-10000
-5000
0
5000
10000
r, km

Fig. 6

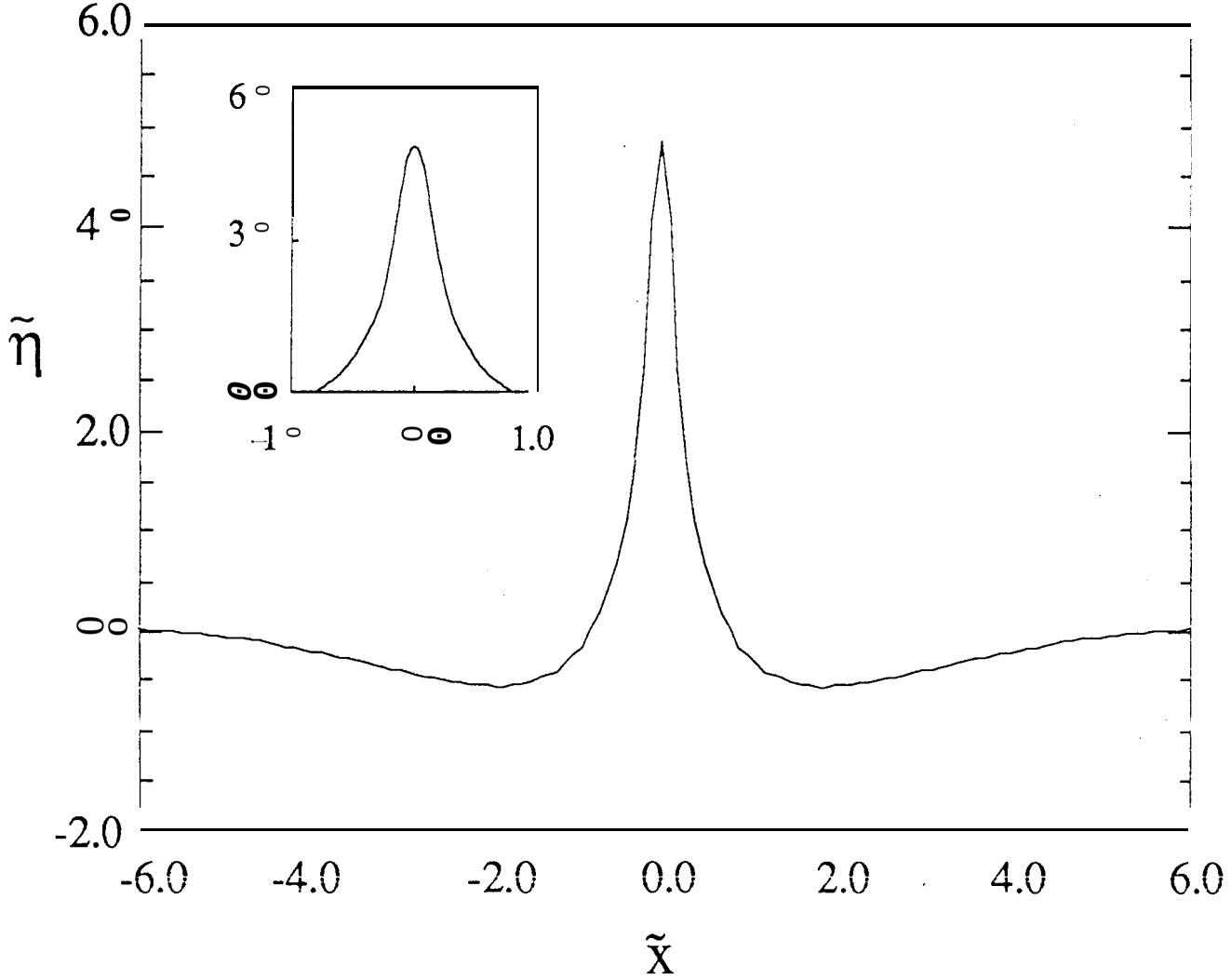

Fig. 7

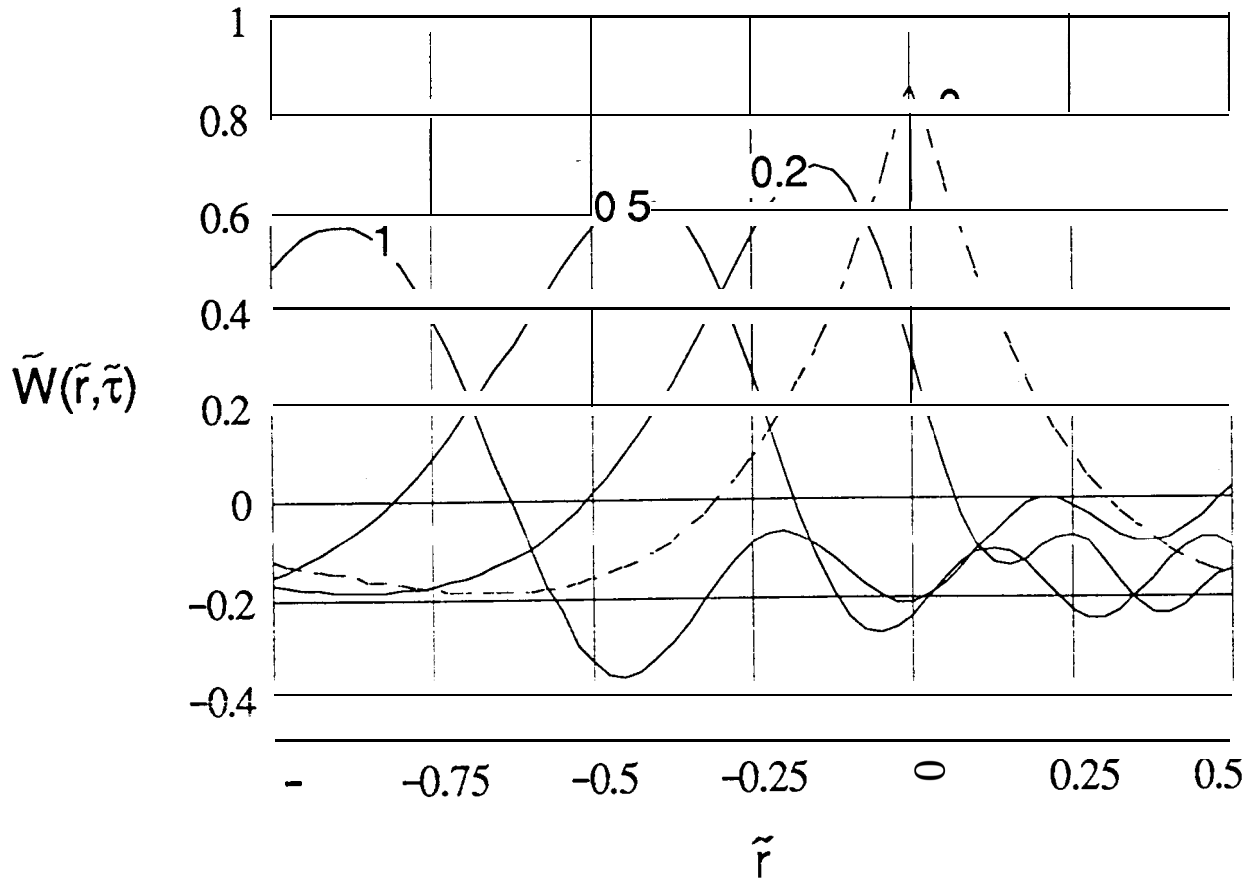

$Q = 3.14,\ \varepsilon = 0.044$

Fig. 8

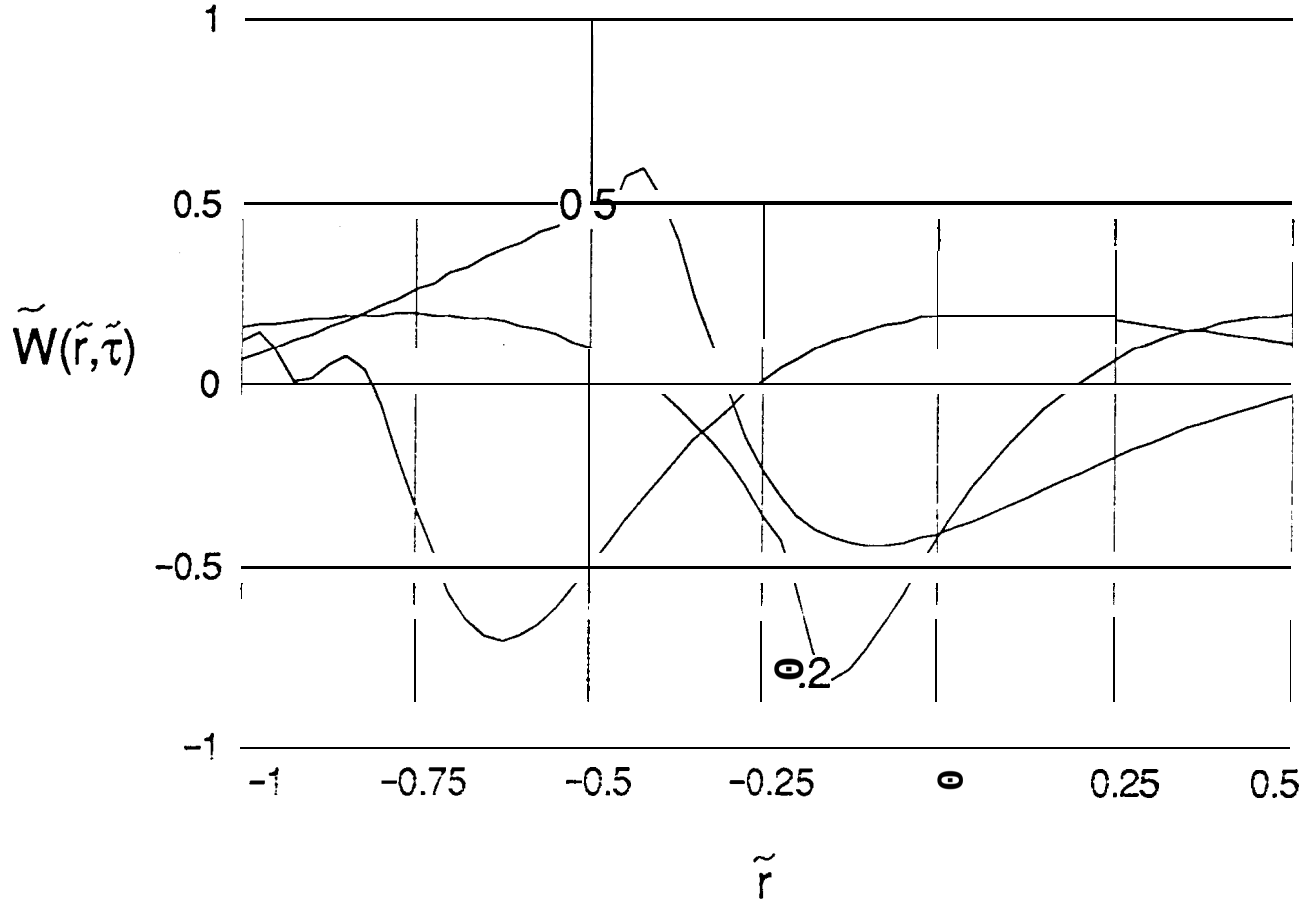

(Q = 3.14, ν = 0.14) Fig. 9